nature portfolio

https://doi.org/10.1038/s41550-021-01570-2

Supplementary information

The origin of underdense plasma downflows associated with magnetic reconnection in solar flares

In the format provided by the authors and unedited

Supplementary Figures or Tables

Parameters and Setup in MHD simulations			
No.	Grids	Magnetic Reynolds Number R_m	Time for Starting 3D (t_0)
Case A	$579 \times 576 \times 288$	5×10^4	17
Case $A_{2.5D}$	579×576	5×10^4	-
Case B	$575 \times 576 \times 288$	10^4	18
Case $B_{2.5D}$	575×576	10^4	-

Table 1: Primary parameters for different cases.

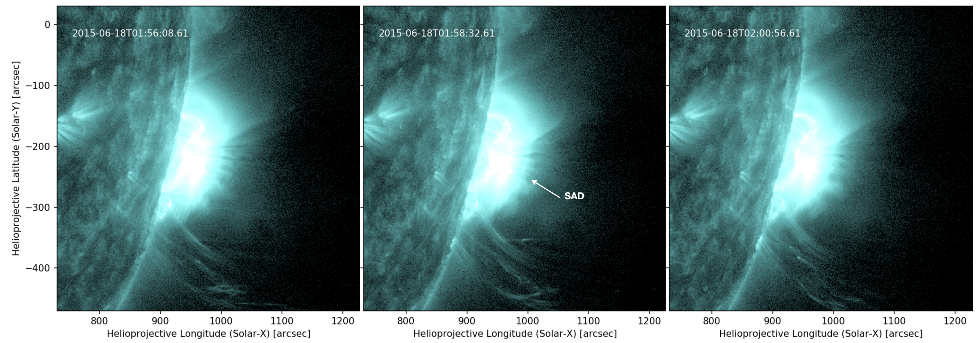

Fig. S1. The example of solar eruptive flare events featuring supra-arcade downflows (SADs). This event is observed by SDO/AIA 131 Å on 2015 June 28 (see the animation in movie s2).

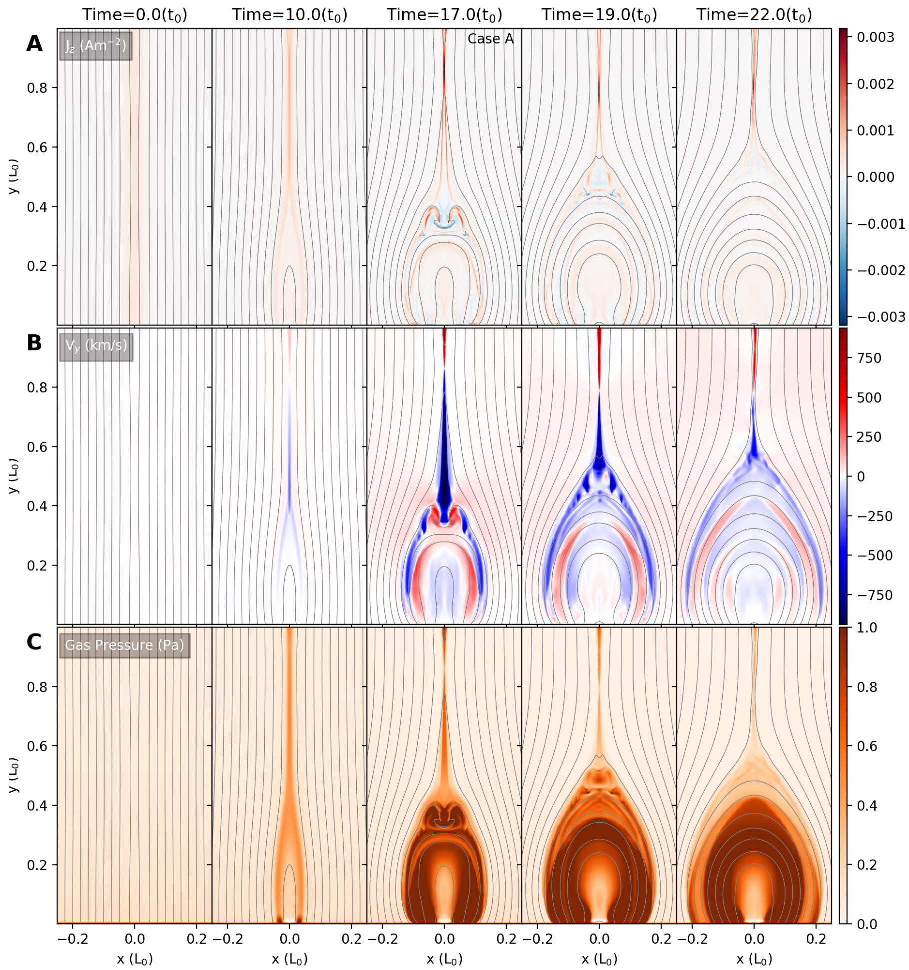

Fig. S2. Evolution of current-density (J_z), velocity component (V_y), and gas pressure (P) in 2.5D simulations for Cases A. The solid curves show the magnetic field lines.

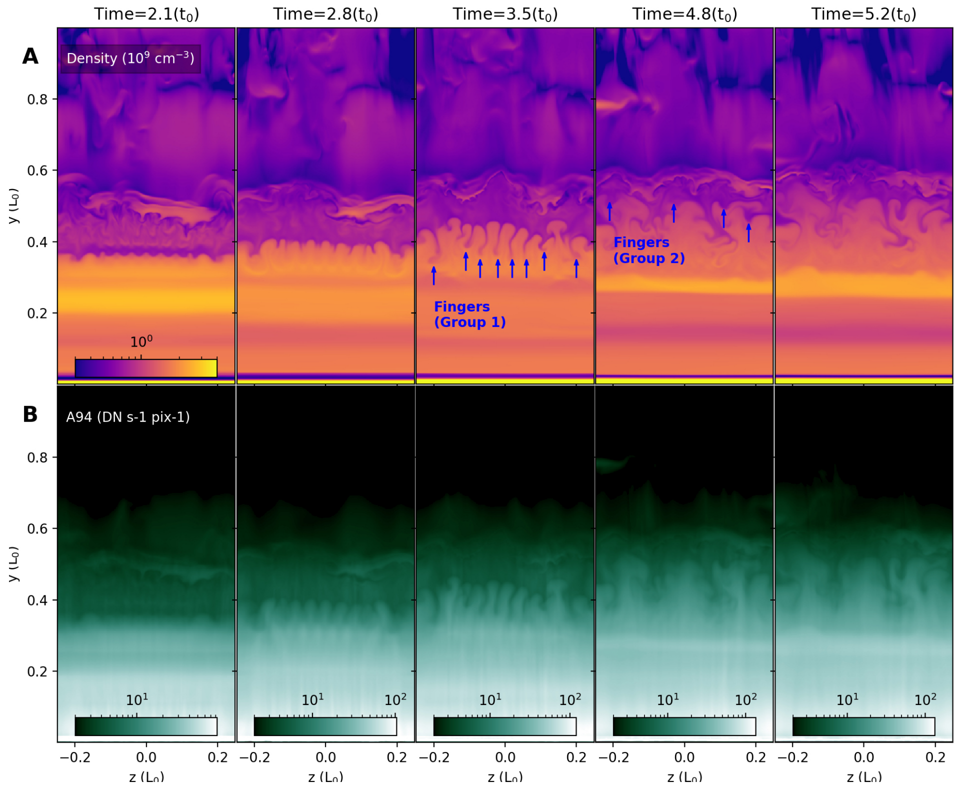

Fig. S3. Temporal evolution of the plasma density and synthetic SDO/AIA 94 Å EUV intensity maps in Case A. This EUV filter-band is sensitive to ∼7 MK flare plasma (through the Fe XVIII line). Arrows indicate Finger-like SAD structures. The finger structures are well-developed until Time=3.5(t_0) as marked by "Group 1", while "Group 2" shows newly formed fingers at the growing bubble surfaces.

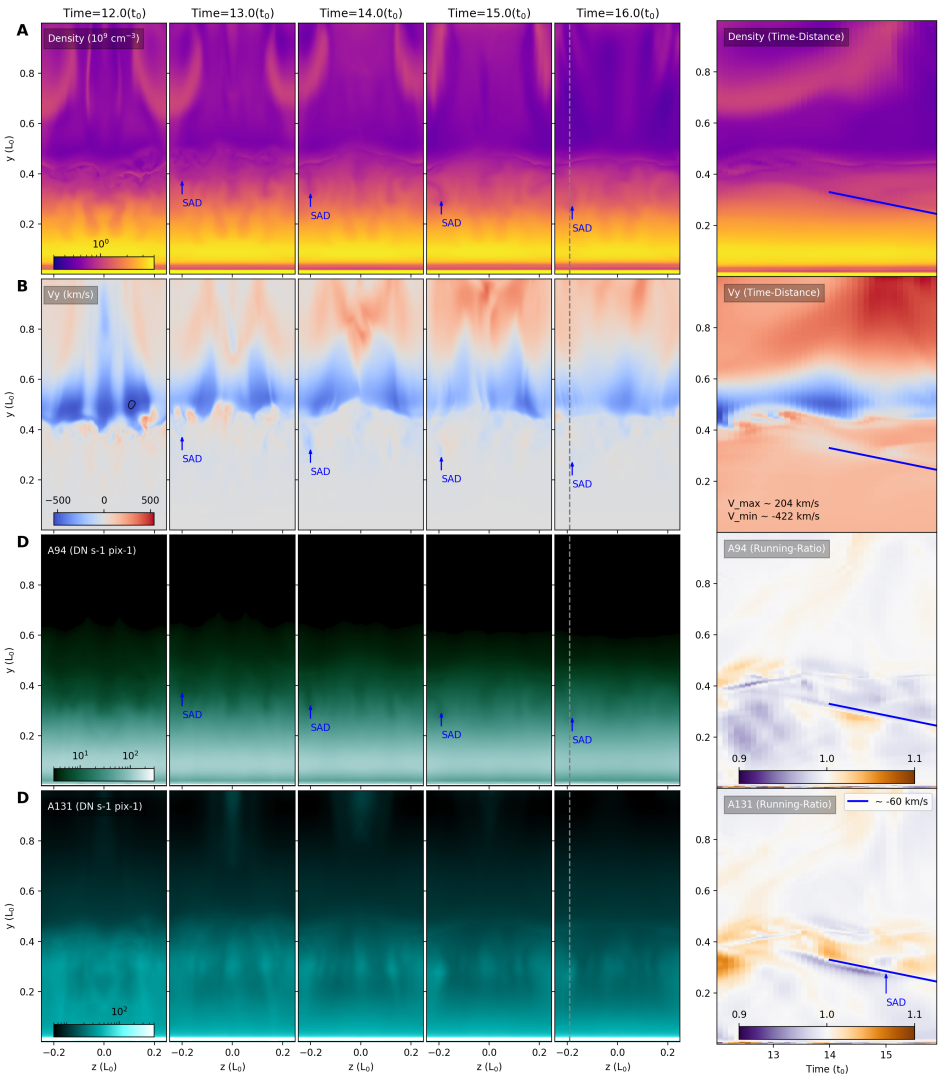

Fig. S4. Temporal evolution of the plasma density, velocity, and synthetic SDO/AIA 94 Å and 131 Å EUV intensity maps in the weak magnetic reconnection regime in Case B. The AIA running ratio images are obtained along the vertical sampling line (z=-0.19 L_0). An example SAD with speed $\sim$ 60 km/s is obtained following the same method as in Fig. 3.

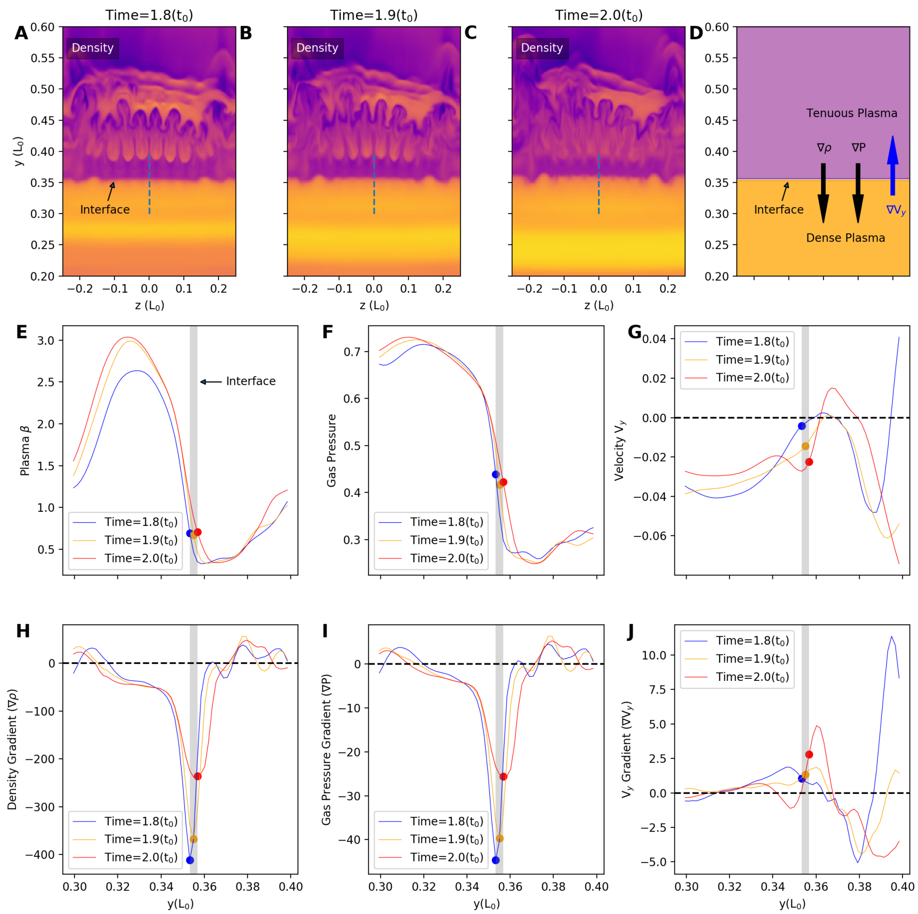

Fig. S5. Initial development of instabilities at the density interface region. (A)–(C) Temporal evolution of the plasma density on the center plane ($x = 0$). (E)–(G) Plasma β, gas pressure, and velocity variation across the interface along the vertical dotted sampling line in (A)–(C). (H)–(J) Density gradient, gas pressure gradient, and velocity (V_y component) gradient along the same sampling line. The blue, orange, and red cycles indicate the density interface height at different times 1.8, 1.9, and $2.0t_0$, respectively. (D) Schematic representation of the direction of the density gradient, gas pressure gradient, and vertical velocity (V_y) gradient. The gray shadows indicate the location of the density interfaces. The positive V_y gradient near the density interface indicates an upward flow towards the tenuous side from the dense plasma side. Both the density gradient and pressure gradient are downwards, which matches the condition for driving the RTI/RMI well.

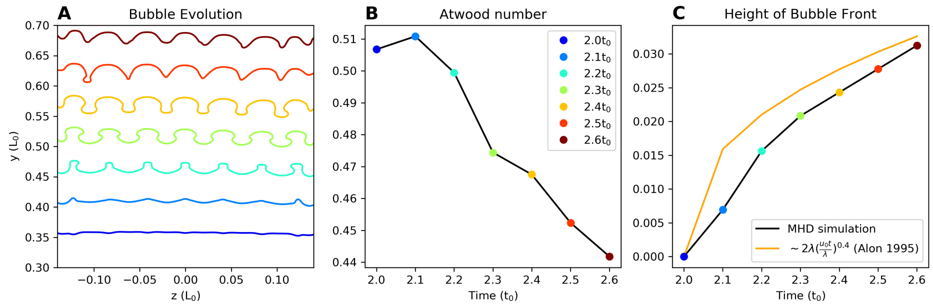

Fig. S6. Bubble evolution during the non-linear RTI/RMI phase. (A) The bubble interface (contours of the density) during the period $2.0-2.6t_0$, vertically offset by a fixed interval $0.05\mathrm{L}_0$ for clarity; (B) The average Atwood number A at different times. Here $A = (\rho_d - \rho_t)/(\rho_d + \rho_t)$, where d and t refer to the dense and tenuous plasma, respectively; (C) Time evolution of the height of the bubbles. The black line is from the MHD simulation, and the orange line is based on a theoretical model[**?**]. Here, the scale-invariant power-law index θ is chosen to be ~ 0.4, the initial perturbation wavelength ($\lambda \sim 0.02$) can be estimated from the panel (A), and the initial perturbation velocity (u_0) is ~ 0.02 based on Fig. S5.

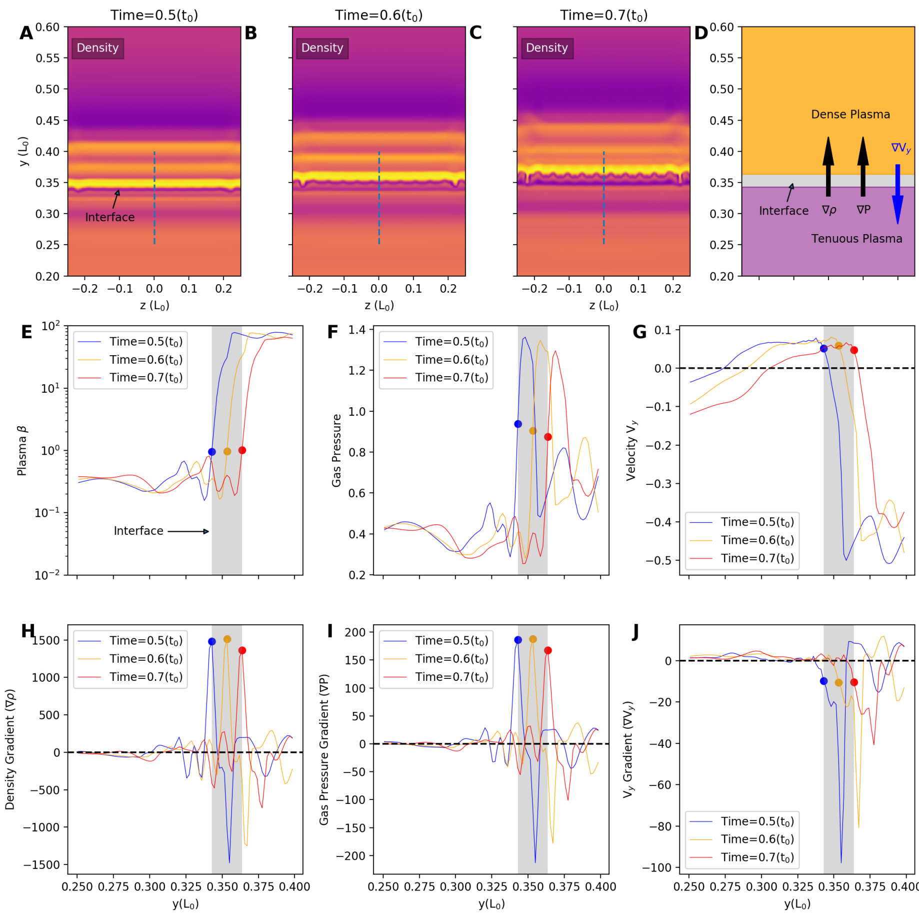

Fig. S7. Development of instabilities at the density interface region with a reversed gradient. Same as Fig. S5 except that the interface appears at early times with a reversed density structure.